Ample textures for electromagnetic scattering in radiative transfer

T. Mathew, B. Rousseau, A. Litman, Y. Favennec

To cite this version:

T. Mathew, B. Rousseau, A. Litman, Y. Favennec. Ample textures for electromagnetic scattering in radiative transfer. Journal of Quantitative Spectroscopy and Radiative Transfer, 2020, 253, pp.107113. 10.1016/j.jqsrt.2020.107113 . hal-02890112

HAL Id: hal-02890112
https://hal.science/hal-02890112v1

Submitted on 15 Dec 2020

Ample textures for electromagnetic scattering in radiative transfer

T. Mathew[a], B. Rousseau[a], A. Litman[b], Y. Favennec[a,*]

[a]*Laboratoire de Thermique et Énergie de Nantes, CNRS UMR 6607, Nantes, France*
[b]*Aix-Marseille Univ, CNRS, Centrale Marseille, Institut Fresnel, Marseille, France*

Abstract

The numerical resolution of wave-matter interaction on complex micro heterogeneities constituting modern industrial materials poses significant computational hurdles. These computations hold a crucial role in the design cycle meant to optimize their participating behavior at high temperatures. To arrive at a reasonable conclusion at the expense of optimal resources, some textural details inherent to these materials are often truncated. For the accurate resolution of multi-scale thermal radiative transport, very little is known today about the role of these truncated textural information to the overall effective radiative properties. With the ultimate prospect of large scale finite element modeling of electromagnetic scattering for participating media, this initial attempt in 2D explores this aspect, learning from the ability of fractals to quantify textural details or roughness of complex objects. Based on a desirable error tolerance, critical quantitative limits were drawn, with which future large scale electromagnetic scattering computations can be performed confidently with optimum resources, without compromising the accuracy. From intensive numerical experiments, ample textural details relevant for a desired accuracy (1 % error) of the extinction efficiency, scattering efficiency, and asymmetry parameter are quantified, and limits established. Error estimates for the aforementioned radiative properties at the limiting resolution (1 µm) of the economical imaging techniques today, are also drawn for better insights.

Keywords: Finite element method, Maxwell's equations, fractals, Koch snowflake, computational electromagnetism

---

[*] yann.favennec@univ-nantes.fr

Preprint submitted to JQSRT *October 26, 2019*

1. Introduction

The accurate modeling of thermal transport in participating media at high temperatures often requires a thorough understanding of radiative transport. Intensive industrial contexts such as aerospace, energy production (solar power plants), etc. deal with materials demanding several antagonist physical (thermo-mechanical, electrical) and chemical properties (oxidation resistance). It appears that considerable efforts are being made today to design advanced materials with an optimal blend of desirable multi-scale properties by introducing particular chemical species. Coupling computer-aided material design strategies, materials with optimum radiative properties can be designed and finely tuned for extreme operating conditions [1].

Major advances have been reported for tailoring macro-porous materials, where local interactions of thermal radiation with internal absorbing/scattering heterogeneities (struts, walls, pores, etc.) were treated with confidence using geometrical optics approximation. The numerical methodologies involved handling 3D digitalized images obtained either through experimental investigation (X-Ray µ-Tomography) or synthetic generation algorithms [2]. The spatial resolution of these X-Ray tomographs ($10-100\,\mu m$) provided Representative Elementary Volumes (REV) for numerical computations capable of predicting radiative quantities in close agreement with experimental observations. However, the significance of hidden or uncaptured micronic details in the multi-scale texture [3] still remains unknown. For materials constituted of micronic heterogeneities, like carbon-fiber based felts, granular ceramics, and agglomerate architectures, the geometrical optics approximation is inadequate to accurately treat their participating behavior.

When textural features are comparable to the wavelength of the exposed radiation, the governing thermal model needs treatment by Maxwell's equations, the fundamental law governing electromagnetic radiation. Resolving Maxwell's equations on arbitrary complex shapes throws significant computational hurdles in terms of resources and time. Valuable insights on demarcating regimes for two-dimensional opaque rough surfaces [4] has helped saving computational resources without compromising accuracy in the past. Though significant conclusions regarding the REV required to homogenize a semi-transparent medium at macro scale exist in literature, very little is known regarding the critical quantitative limit or resolution of micro textures for general two- and three-dimensional entities.

Wave-matter interaction at micro-scales has always been an occupied domain of research, especially with regard to isolated or co-related particles of arbitrary cross-section [5]. When non-regular or complex shaped micro heterogeneities are to be treated, researchers tend towards numerical methods for an approximate solution, whose accuracy greatly depends on the input geometry and its inherent textural details. The influence of cross-sectional shape [6] of these micro-heterogeneities on the overall effective radiative properties is not well-known today. There exist considerable computational challenges for the resolution of Maxwell's equations with numerical methods like the finite element method [7], popular in the scientific computing community for its ease of handling complex computational domains. For an optimal computational resource and time, a blind approximation is often done to the input geometry and its inherent textural details, which can be detrimental without a critical limit. Worth mentioning the level of accuracy desirable in a specific domain of interest, this work with a finite element framework narrows this gap of uncertain assumptions with quantitative conclusions.

The developed finite element framework is employed on Koch snowflake fractals as an initial step in this endeavor. Fractals, mostly termed as a blend of simplicity and complexity, are popular in computer graphics and imaging, to recreate real-world complex entities on finite pixels in memory. Learning from the ability of fractals to quantify and characterize textural parameters or roughness of complex objects, this work attempts to ponder an appropriate quantitative limit or resolution of textures for a desired accuracy, beyond which any further improvement ceases to – or has negligible influence on the effective radiative properties of participating media with micro-heterogeneities. To account for all the geometrical orientations of the scatterer, and to ensure confidence on the quantitative limits derived for a material across the desired spectrum, this work which is also an extension of [8] involved intensive numerical experiments. Each scatterer dealt in this work has been treated with 6 angle of incidences (after accounting for the possible geometrical symmetries), and a very fine spectrum of wavelength (100 data points in $[4, 25]$ µm corresponding to 300 K) for both silicon carbide and silica in both transverse electric (TE) and transverse magnetic (TM) mode. Silica being a prototype for a semi-transparent material [9, 10, 11] and silicon carbide for opaque material [12] for usual thickness ensures a general material perspective to the study. All possible physical scenarios related to single scatterers, to the best of our knowledge, have been accounted while tailoring the numerical experiments and these considered scenarios are treated with extreme practical precision to arrive at accurate critical limits.

The paper is organized as follows: Section 2 introduces the mathematical model underlying the modeled physical phenomenon: electromagnetic scattering. The governing partial differential equations for the total-scattered field formulation and the associated boundary conditions are detailed for both mode of polarization dealt in this work, followed by the weak formulation for approximation by the finite element method. Having discussed the numerical model to obtain the scattered field, the empirical relations to compute the interested radiative properties are detailed. This section concludes with a discussion on the Koch snowflake fractal employed in this work. Section 3 presents the results obtained from attempted numerical experiments; evaluates the scattering phenomena of fractals leading to a critical limit. A wide spectral range from 4 to 25 µm discretized into 100 discrete wavelengths is considered to ensure the reliability of estimated limits; with 2 media: optically thick, and optically thin; in 2 transverse modes: transverse electric (TE) and transverse magnetic (TM); at 6 different angles of incidences; for 3 different fractal sizes, totaling $43,200$ simulations. This section concludes with quantitative limits for each medium where the error associated with the investigated radiative properties are enumerated. It is found that a resolution of 1 µm yields around 1 % error in averaged radiative properties in the TE mode, while this error is slightly more in the TM mode. Section 4 gathers all the critical observations and emphasize the critical limits or associated error obtained. This section concludes by discussing possible extensions and future perspectives.

2. Methodology

The physical process termed electromagnetic scattering occurs when an electromagnetic wave interacts with a heterogeneity in the medium it propagates. This heterogeneity often referred to as scatterer can be a particle with refractive index different than the surrounding. The fundamental objective underlying the study of an electromagnetic scattering problem is to understand and quantify the energy transformation during this wave-matter interaction. This exchange of energy or *extinction* is due to *scattering*, which involves re-radiating the energy of the incident wave to newer directions, and *absorption*, which involves transformation of energy into other forms, like thermal. Maxwell's equations govern this physical phenomenon, and the energy exchange involved can be quantified by resolving these equations for the investigated medium.

2.1. Mathematical model

Assuming source-free conditions, a 2D z-invariance, and the harmonic propagation of the wave in the z-direction, the governing model of wave-matter interaction for a non-magnetic medium characterized by the permittiviy ϵ_r is given by,

$$-\Delta E - k_0^2 \epsilon_r E = 0, \tag{1}$$

the Helmholtz equation which links the electromagnetic field with frequency ω, $k_0 = \omega\sqrt{\mu_0 \epsilon_0}$ the free-space wave number, and ϵ_r the complex-valued relative permittivity of the medium from the complex refractive index of the medium $\tilde{n} = n + \mathrm{i}\kappa$, as $\epsilon_r = \tilde{n}^2$. The problem statement investigated in this work is developed on the total-scattered field formulation, widely used in computational electromagnetics [13]. The formulation search for the scattered field E_s by exciting the scatterer Ω_s characterized by ϵ_s with an incident field E_i at the boundary Γ', as shown in fig. 1, such that $\Omega' \cup \Omega_s \subset \Omega$ models the total field $E = E_i + E_s$.

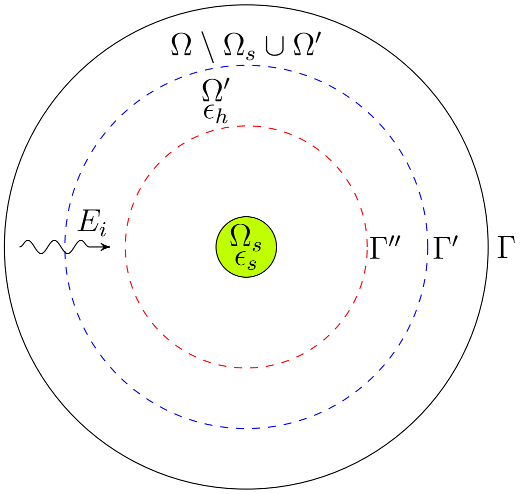

Figure 1: total-scattered field formulation

The mathematical statement of the scattering problem governing the transverse electric (TE) scattered field E_s in the computational domain Ω

bounded by Γ is enumerated as:

$$\begin{aligned} -\Delta E_s - k_0^2 \epsilon_r E_s &= 0, && \text{in } \Omega \setminus \Omega_s \cup \Omega', && \text{(2a)} \\ -\Delta E_s - k_0^2 \epsilon_r E_s &= k_0^2(\epsilon_r - \epsilon_h) E_i, && \text{in } \Omega_s \cup \Omega', && \text{(2b)} \\ \partial_n E_s &= \mathrm{i} k_0 E_s, && \text{on } \Gamma, && \text{(2c)} \end{aligned}$$

where ϵ_h is the complex permittivity of the host medium ($\epsilon_h = 1$ for vacuum). Note that first order absorbing boundary conditions truncate the computational domain at Γ. The analogous statement of the scattering problem governing the transverse magnetic (TM) scattered field E_s is:

$$\begin{aligned} -\frac{1}{\epsilon_r}\Delta E_s - k_0^2 E_s &= 0, && \text{in } \Omega \setminus \Omega_s \cup \Omega', && \text{(3a)} \\ -\frac{1}{\epsilon_r}\Delta E_s - k_0^2 E_s &= \left(\frac{1}{\epsilon_h} - \frac{1}{\epsilon_s}\right)\Delta E_i, && \text{in } \Omega_s \cup \Omega', && \text{(3b)} \\ \partial_n E_s &= \mathrm{i} k_0 E_s, && \text{on } \Gamma, && \text{(3c)} \end{aligned}$$

2.2. Numerical model

The aforementioned mathematical model eq. (1) can be resolved analytically only on regular geometries. Numerical methods are sought for an approximate solution as the geometrical complexity increases. Detailed surveys of existing numerical methods for scattering are available in the literature like [14, 15, 16], emphasizing the mathematical setting, pros and cons of popular techniques like discrete dipole approximation (DDA), etc. Owing to the ease of resolving partial differential equations on complex computational domains, the finite element method has been chosen in this work. Contrary to the popular finite difference method where the partial differential operator is approximated, the finite element method approximates the functional spaces in which the solution is searched for. Choosing appropriate functional space $\mathcal{H}^1(\Omega) = \{u \in \mathrm{L}^2(\Omega), |\nabla u| \in \mathrm{L}^2(\Omega)\}$, the variational statement for the TE mode involves finding $E_s \in \mathcal{H}^1(\Omega)$ such that,

$$\begin{aligned} &\int_{\Omega} \nabla V^* \cdot \nabla E_s - k_0^2 \epsilon_r V^* E_s \, \mathrm{d}\boldsymbol{x} - \mathrm{i} k_0 \int_{\Gamma} V^* E_s \, \mathrm{d}\boldsymbol{x} \\ &\qquad = k_0^2 \int_{\Omega' \cup \Omega_s} (\epsilon_s - \epsilon_h)\; V^* E_i \, \mathrm{d}\boldsymbol{x}, \ \forall \ V \ \in \mathcal{H}^1(\Omega), \qquad (4) \end{aligned}$$

where * denotes the complex conjugate. The analogous statement in the TM mode involves finding $E_s \in \mathcal{H}^1(\Omega)$ such that,

$$\begin{aligned} &\int\limits_{\Omega} \frac{1}{\epsilon_r} \nabla V^* \cdot \nabla E_s - k_0^2 V^* E_s \, \mathrm{d}\boldsymbol{x} - \frac{1}{\epsilon_r} \mathrm{i} k_0 \int\limits_{\Gamma} V^* E_s \, \mathrm{d}\boldsymbol{x} \\ &= \int\limits_{\Omega' \cup \Omega_s} \left(\frac{1}{\epsilon_h} - \frac{1}{\epsilon_s} \right) \nabla V^* \cdot \nabla E_i \, \mathrm{d}\boldsymbol{x}, \, \forall \, V \, \in \mathcal{H}^1(\Omega), \end{aligned} \tag{5}$$

Owing to the sparsity of the linear system obtained from the discrete variational problem, large scale computational domains can be attempted at the expense of computational resource and time. The problems in computational electromagnetics demand a minimum level of discretization of the domain for the interested wavelength. This criterion can be detrimental at the visible spectrum considering the requirement of the first order Lagrange polynomial basis ($\mathcal{P}_1$) demanding at least 20 elements per wavelength ($\frac{\lambda}{20}$). The second order counter-part, ($\mathcal{P}_2$), demands only $\frac{\lambda}{10}$, which can be favorable considering that providing a coarser triangulation of the domain will be efficient in terms of memory and time for parallel large-scale computations. This coarsening can scrape off some relevant textures from the studied scatterer(s) contributing the accuracy, for which a quantitative critical limit can help implement the coarsening confidently. Although some uncertain assumptions can be derived from the current physical insights with the regard to the involved size parameter ($\frac{\pi d'}{\lambda}$), d' being the characteristic dimension of the scatterer, some stronger quantitative conclusions are to be drawn for further large-scale computations on scatterer(s) with fine textural details. The critical limit particular to a medium at the interested spectrum is also more reliable for accuracy than vague physical assumptions. Although the modern finite element libraries benefit from advanced programming data structures and communication paradigms, the finite computational resources can demand a compromise for the input triangulation because of memory and mesh generation constraints, especially in 3D. The number of elements in the triangulation of a spherical domain with a radius of 15 µm for solving a problem involving wavelength of 5 µm (with a maximum element size: $\frac{\lambda}{20} = 0.25$) is approximately 30 million tetrahedrons. The triangulation of the interested micro-structures coming from popular imaging techniques involve significant challenges which need serious re-meshing and pre-processing strategies. Though splitting the coarsened input triangulation after partitioning and distribution is a viable strategy, the splitting cannot account for the truncated textures while coarsening. This work originates at this impasse, where the authors plan massively parallel and large scale electromagnetic scattering computations for the micro-scale analysis of numerous industrial materials at visible and infra-red spectrum.

2.3. Radiative properties

In electromagnetism, the Poynting vector represents the energy carried by an electromagnetic wave and the time-averaged Poynting vector for time-harmonic fields represents the energy flux given by:

$$\mathbf{S} = \frac{1}{2}\Re[\mathbf{E} \times \mathbf{H}^*], \qquad \left[\mathrm{W/m^2}\right]. \tag{6}$$

With the knowledge of the scattered field E_s, the energy transformation can be quantified in terms of the cross-section, which is defined as the ratio of the net rate at which the electromagnetic energy [W] crosses the boundary Γ'' centered at the scatterer, to the incident energy $\mathbf{S}_i = \frac{1}{2\eta}|E_i|^2\hat{\mathbf{k}_\theta}$ [W/m^2], where $\eta = \sqrt{\frac{\mu}{\epsilon}}$ is the characteristic impedance of the medium, and $\hat{\mathbf{k}}_\theta = [\cos\theta, \sin\theta]$ is the direction of the incident plane wave. The scattering cross-section c_s relates the amount of power removed from the incident wave as a result of scattering, which involves re-radiating the energy of the incident wave to new directions [17]. It is given by:

$$c_s = \frac{\oint\limits_{\Gamma''} \mathbf{S}_s \cdot \hat{\mathbf{n}}}{\mathbf{S}_i}, \qquad \text{where } \mathbf{S}_s = \frac{1}{2}\Re[\mathbf{E}_s \times \mathbf{H}_s^*], \tag{7}$$

where $\hat{\mathbf{n}}$ is the unit vector normal to Γ''. The extinction cross-section accounting the overall energy exchange, the scattering and absorption losses, during the wave-matter interaction is given by,

$$c_e = \frac{\oint\limits_{\Gamma''} \mathbf{S}_e \cdot \hat{\mathbf{n}}}{\mathbf{S}_i}, \qquad \text{where } \mathbf{S}_e = \frac{1}{2}\Re[\mathbf{E}_s \times \mathbf{H}_i^* + \mathbf{E}_i \times \mathbf{H}_s^*]. \tag{8}$$

The respective efficiencies for a scatterer of geometrical cross-section c_g is given by:

$$Q_s = \frac{c_s}{c_g}, \tag{9}$$

$$Q_e = \frac{c_e}{c_g}. \tag{10}$$

The asymmetry parameter g quantifying the mean direction of scattered light, is defined as the average of the scattering angle weighted to the scattered power, given by:

$$g = \frac{\oint\limits_{\Gamma''} \hat{\mathbf{n}} \cdot \hat{\mathbf{k}}_\theta \; (\mathbf{S}_s \cdot \hat{\mathbf{n}})}{\oint\limits_{\Gamma''} \mathbf{S}_s \cdot \hat{\mathbf{n}}}. \tag{11}$$

2.4. Koch snowflake

Koch snowflake, a fractal curve based on the Koch curve [18] is constructed by recursively altering line segments in steps starting from an equilateral triangle. The initial curve, the equilateral triangle, is recursively iterated ℓ times, leading to the fractal K^ℓ, whose perimeter increases with ℓ. To compare the fractals generated in the consecutive iterations pertain to a scatterer with given cross-section $c_g = d'$ and size parameter, fractals of same cross-sectional area have been generated for consecutive levels. The fractals with a given cross-sectional area d' [µm] will be denoted as belonging to the set $F_{d'}$, where d' is the diameter of the cylinder with equivalent cross-sectional area. Figure 2 shows the fractals $F_{d'}$ obtained for 5 consecutive levels.

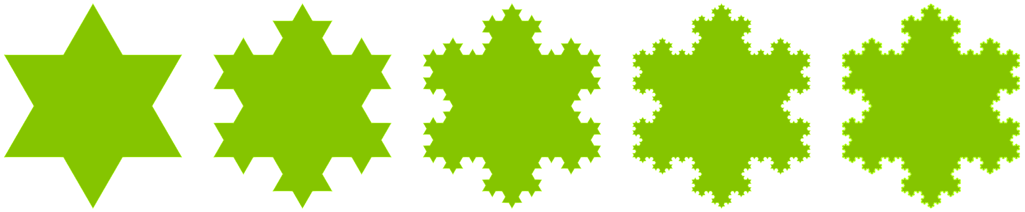

K^1 K^2 K^3 K^4 K^5

Figure 2: Koch snowflake fractals $K^\ell \in F_{d'}$, $\ell = \{1, 2, 3, 4, 5\}$

3. Results and discussion

The numerical models eqs. (4) and (5) have been implemented in the open-source finite element domain specific language FreeFEM, which is a partial differential equation solver [19] written in C++. With the ultimate objective of large scale resolution of Maxwell's equations, an in-house numerically validated parallel solver has been developed both in 2D and 3D.

The resulting linear system is so huge for the electromagnetic spectrum of interest, iterative methods based on domain decomposition and message passing interface (MPI) is relied through the open-source linear algebra library HPDDM [20]. The numerical experiments have been attempted on silicon carbide and silica fractals, an optically thick and thin medium, respectively of three different sizes (d') for the spectral range 4 µm to 25 µm. The optical properties $\tilde{n} = n + \mathrm{i}\kappa$ of the studied materials across the aforesaid spectral range is plotted in fig. 3.

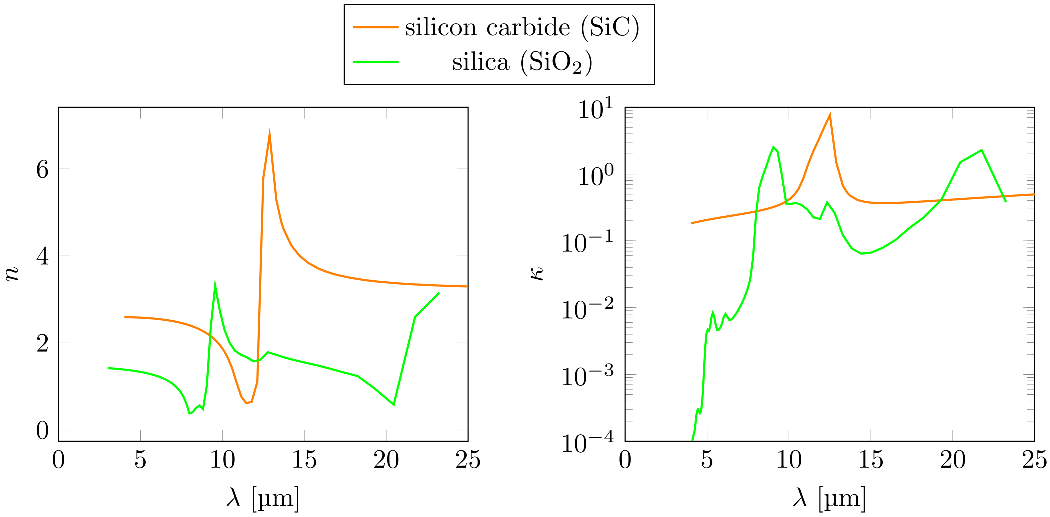

Figure 3: optical properties of silicon carbide and silica across the interested spectrum

Table 1 lists the length of the smallest segment $\widetilde{h}$ of all fractals K^ℓ dealt with in this work. The triangulation of the domain Ω with element size $\hat{h} < \frac{\lambda}{20}$ for convergence has been generated using the open-source finite element mesh generator Gmsh [21]. First order Lagrange conforming finite element basis

	K^1	K^2	K^3	K^4	K^5
F_6	2.33268	0.737658	0.240598	0.0794514	0.0263752
F_{18}	6.99804	2.21297	0.721793	0.238354	0.0791257
F_{54}	20.9941	6.63892	2.16538	0.715063	0.237377

Table 1: length of the smallest segment $\widetilde{h}$ of fractal $K^\ell \in F_{d'}$, in [µm]

is employed to obtain the linear system. The resulting linear system has been resolved with a parallel direct solver in the open-source linear algebra package PETSc [22]. To ensure the physical reliability of conclusions drawn from this work, intensive numerical experiments involving: 2 materials × 2 modes × 6 angle of incidences × 100 wavelengths in $[4, 25]$ µm × 18 scatterers (6 geometries (5 fractals and 1 cylinder) × 3 diameters: $d' = \{6, 18, 54\}$). In total, $43, 200$ solves have been attempted. Each solve was done on 100 MPI processes where timings range with fractal size from 10 to 400 s. A plane wave propagating in the $+x$ direction $E_i = e^{\mathrm{i}k_0 x}$ – adopting the sign convention for the complex index of refraction $\tilde{n} = n + \mathrm{i}\kappa$, excites the problem. Scattering in free space ($\epsilon_h = 1$) is dealt with in this work.

3.1. Total field plots

The modulus of the total field $|E| \in \mathcal{H}^1(\Omega)$ obtained by the superposition of the incident field E_i and scattered field E_s for silicon carbide fractals at 4 µm in the TE mode is plotted in fig. 4. To have a clear distinction between each level K^ℓ for a particular size $F_{d'}$, the plots for each size $F_{d'}$ have individual scales. This aids in identifying the differences in scattering patterns across each level more clearly. The scattering pattern or nature of silicon carbide fractals shows convergence at K^3 irrespective of the fractal size d' (the computed total electric field and the scattering pattern clearly change from K^1 to K^3, as can be seen in fig. 4, while the scattering pattern seems to stabilize from K^3 to K^5). This initial observation implies that the subsequent smaller and additional details present on the scatterer is not significantly influencing their near-field scattering. These scattering plots can also serve as a starting point for further studies involving multiple scatterers. The respective plots for silica fractals are shown in fig. 5. Contrary to silicon carbide, the scattering pattern of silica fractals seem to rather converge at K^4. This difference between the optically thick and thin medium implies the need of a critical limit specific to the medium of interest, and further motivates the investigation in terms of other desired radiative properties.

3.2. Far-field plots

Inferring the near-field behavior, the far-field patterns around the studied fractals have been plotted in the TE mode at 4 µm following the near-field to far-field transformation based on surface equivalence theorem [23]. After taking into account the geometrical symmetry of the fractals (every 60°), the far-field patterns for a set of angle of incidence ($\theta = 0°$, $20°$, and $30°$) are plotted. The far-field plots of the fractals have also been compared against the equivalent circular cylinder with same cross-sectional area, as shown in figs. 6 and 7. The far-field behavior also shows a global convergence at $K^3 -$ irrespective of the size, material or angle of incidence (the modulus of the electric far-field and the pattern clearly have differences from K^1 to K^3, as can be seen in figs. 6 and 7, while this seems to stabilize from K^3 to K^5). The more pronounced scattering differences for the bigger fractals, as observed from both the near-field and far-field plots, also agrees with the existing literature [6]. The discussed near-field and far-field plots at 4 µm portraying the local spectral behavior is meant only for some initial qualitative assessments. To realize more substantial conclusions across the spectrum for the radiative properties of interest, results from intensive computations are detailed next.

3.3. Radiative properties across the spectrum

To infer a quantitative limit specific to a material across the spectrum of interest regarding the influence of fine details on the desired radiative properties, the evolution of extinction efficiency, scattering efficiency and asymmetry parameter have to be known across the spectral range. To account for the polarization effects, the properties extracted from both TE and TM mode computations are shown. The radiative properties averaged across 6 angle of incidences have been plotted to take into account the different fractal orientations with respect to the incident radiation ($\theta = \{0°, 10°, 20°, 30°, 40°, 50°\}$). The averaged extinction efficiency $\widehat{Q}_e = \dfrac{1}{\dim\theta}\sum_i Q_e^i$ is computed, with Q_e^i the extinction efficiency Q_e for i^{th} angle of incidence, and with $\dim\theta = 6$. Plots for all the attempted test cases are shown in fig. 8 (note that each plots are in their individual scale than a common scale for clear distinction between each level).

The plots of extinction efficiency for all the investigated sizes (apparent diameter $d' = \{6, 18, 54\}$; optically thick and optically thin media; transverse electric and transverse magnetic modes) show convergence at K^3. The deviation of the respective plots for fractals from those for the equivalent cylinders seems to be more significant for optically thick scatterers. Respective plots for averaged scattering efficiency $\widehat{Q}_s$ and averaged asymmetry parameter $\widehat{g}$, portraying the associated scattering, are shown in fig. 9 and fig. 10, respectively. For these properties also, a convergence around K^3–K^4 is observed.

3.4. Critical limit

For estimating a critical quantitative limit specific to a material, based on an allowable error tolerance, an error criterion based on K^5, the fractal with 3072 line segments and finest details was defined. From this, the associated error in each investigated radiative property can be determined for all the involved test cases. This also helps to quantify the textural details required for an accurate resolution of the investigated radiative property. To arrive quantitatively at a critical limit $\widetilde{h}_\varepsilon$ for a desired accuracy, we define the wavelength-averaged normalized error,

$$\varepsilon = \sqrt{\frac{\sum_i \left(u^\ell(\lambda_i) - u^5(\lambda_i)\right)^2}{\sum_i \left(u^5(\lambda_i)\right)^2}} \quad \forall F_{d'}, \tag{12}$$

where $u^\ell = \{\widehat{Q}_e,\ \widehat{Q}_s,\ \widehat{g}\}$ are the averaged radiative properties for the fractal K^ℓ, characterized by a minimum segment length $\widetilde{h}$ as tabulated in table 1. $u^\ell(\lambda_i)$ is compared against those for the reference fractal K^5, $u^5(\lambda_i)$, $\forall F_{d'}$ across the spectrum. The associated error ε in radiative properties for all fractals studied $F_{d'}, d' = \{6, 18, 54\}$ in the TE mode are plotted in fig. 11. It appears that the error ε increases with the minimum segment length $\widetilde{h}$, for all average radiative properties, for the two media, as expected [6]. Detailed data pertaining to all the test cases studied – both in TE and TM mode, are also tabulated in tables 2 and 3. These tables serve as a lookup information for a specific material, that error associated for a particular radiative property can be related to the available textural information. For a desirable error tolerance ε of 1 %, a quantitative limit $\widetilde{h}_\varepsilon$ has been derived. This critical limit is tabulated in table 2 and is also shown as $\widetilde{h}$ limit of the yellow shaded portion in the respective plots of fig. 11. The blank cells that appear in table 2 imply that no critical limit met the 1 % error tolerance. It is worthwhile to note that for the given desirable error tolerance of 1 %, the critical limits for different radiative properties are different for each material. From this table of information, appropriate critical limits can be chosen confidently with the objective of an interested radiative property: approximately, 1 % error tolerance yields critical limits varying around 1 µm, and, in any case, less than 4.5 µm. Also to mention that this lookup information for a given material can also provide the likelihood of the associated error for a given resolution of textural details, see table 3, and the blue shaded portion in plots of fig. 11. The textural resolution of 1 µm yields maximum errors of approximately 1 % for both TE and TM modes, for both optically thick and thin media, for the extinction efficiency, scattering efficiency, and asymmetry parameter. These quantitative error estimates can also provide and facilitate with better understanding of the relative relevance of textural information in the associated energy exchange.

Material	TE			TM		
	$\widehat{Q}_e$	$\widehat{Q}_s$	$\widehat{g}$	$\widehat{Q}_e$	$\widehat{Q}_s$	$\widehat{g}$
SiC	4,32	1,72	1,11	3,31	-	-
SiO_2	1,15	1,00	1,94	1,36	0,91	0,78

Table 2: Critical limits $\widetilde{h}_\varepsilon$ [µm] for 1 % wavelength-averaged normalized error tolerance, corresponds to $\widetilde{h}$ limit of the yellow shaded region in fig. 11. Note that the blank cells that appear for the TM mode imply that no critical limit met the 1 % error tolerance. Note also that the union of yellow and blue colors yields the green color.

Material	TE			TM		
	$\widehat{Q}_e$	$\widehat{Q}_s$	$\widehat{g}$	$\widehat{Q}_e$	$\widehat{Q}_s$	$\widehat{g}$
SiC	0,82	1,12	1,23	2,70	7,11	5,57
SiO_2	1,52	1,38	0,78	1,68	2,12	1,85

Table 3: Maximum wavelength-averaged normalized error [%] that can occur at 1 µm resolution, corresponds to the ε limit of the blue shaded region in fig. 11. Note that the union of yellow and blue colors yields the green color.

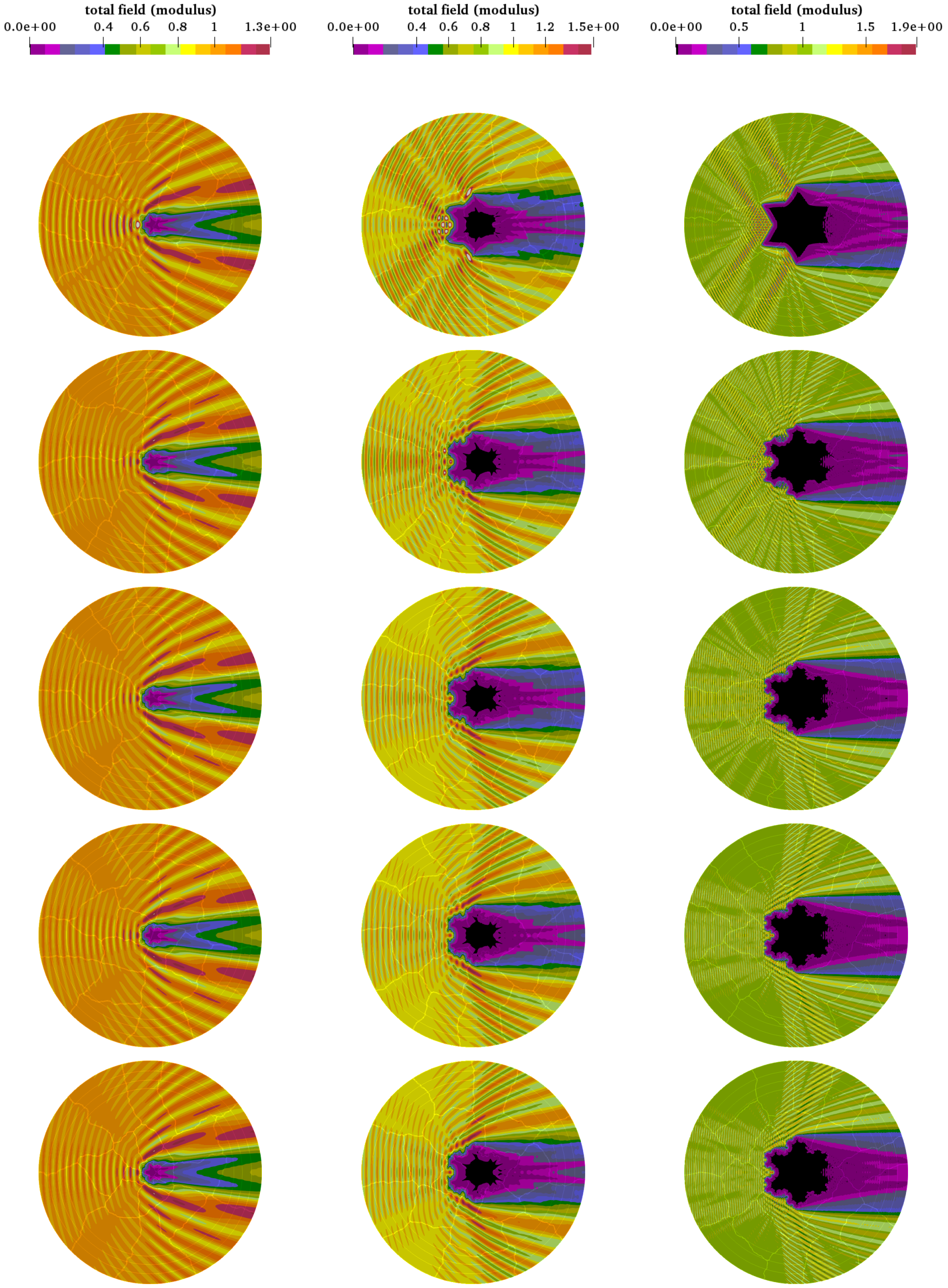

F_6 F_{18} F_{54}

Figure 4: Modulus of the total electric field $|E| \in \mathcal{H}^1(\Omega)$ for silicon carbide at $\lambda = 4\,\mu\text{m}$ in TE mode. Top row corresponds to K^1, subsequent rows correspond to K^2, K^3, K^4, and K^5, respectively.

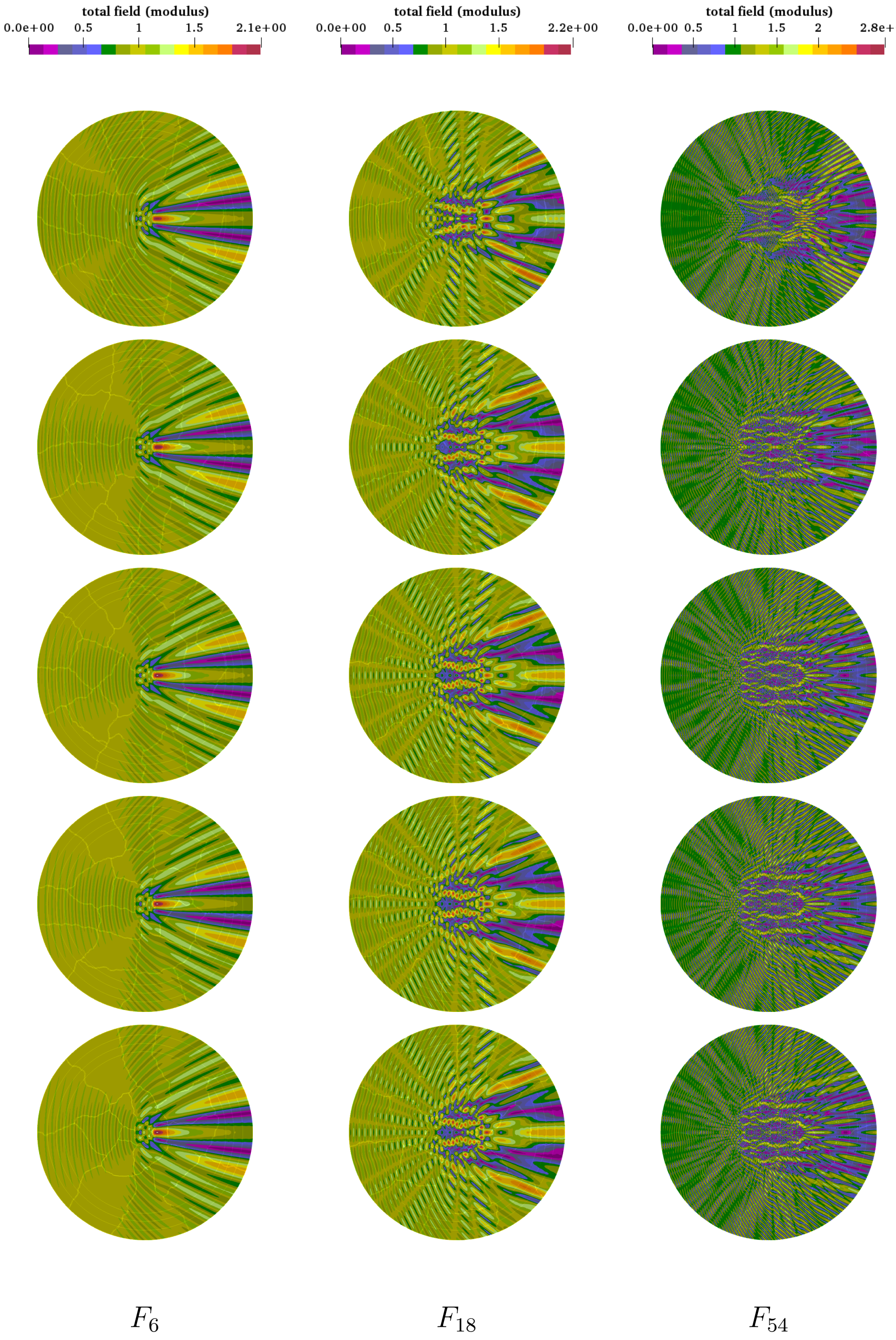

Figure 5: Modulus of the total electric field $|E| \in \mathcal{H}^1(\Omega)$ for silica at $\lambda = 4\,\mu\text{m}$ in TE mode. Top row corresponds to K^1, subsequent rows correspond to K^2, K^3, K^4, and K^5, respectively.

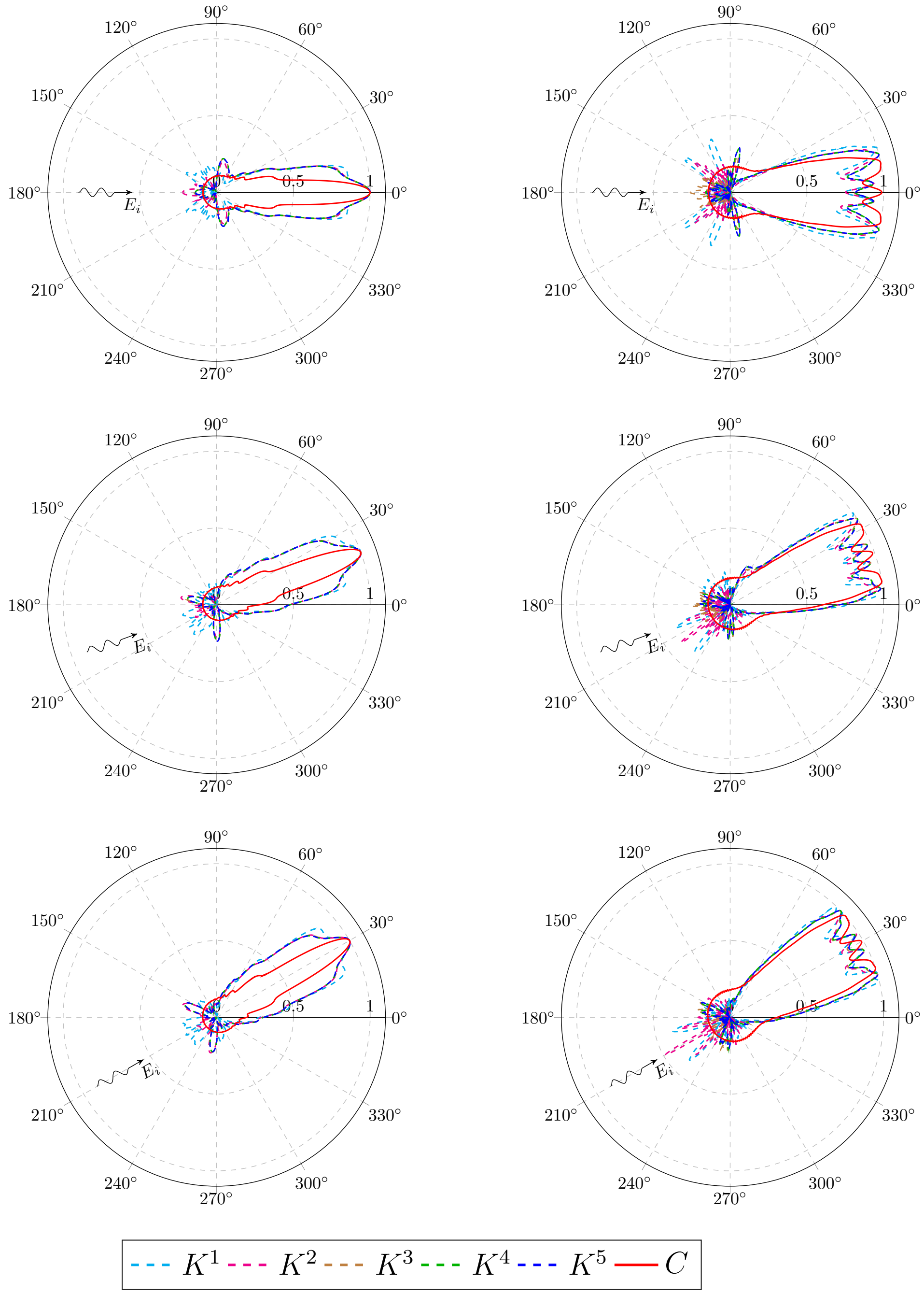

Figure 6: Modulus of electric far-field at 4 µm in the TE mode for silicon carbide scatterers F_{18} (left) and F_{54} (right). Top row corresponds to excitation at 0° angle of incidence, the second and third row corresponds to 20° and 30°, respectively.

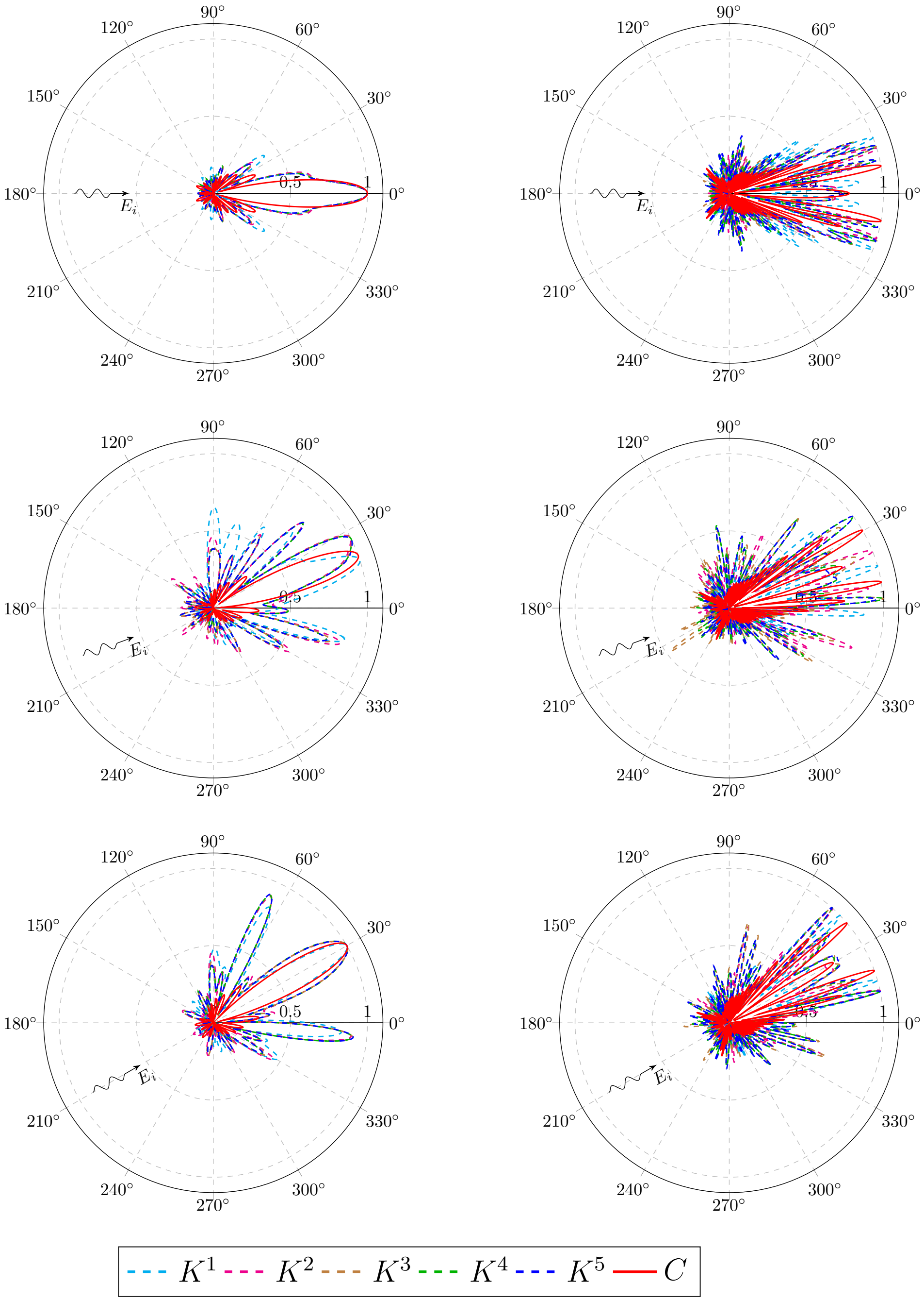

Figure 7: Modulus of electric far-field at 4 µm in the TE mode for silica scatterers F_{18} (left) and F_{54} (right). Top row corresponds to excitation at 0° angle of incidence, the second and third row corresponds to 20° and 30°, respectively.

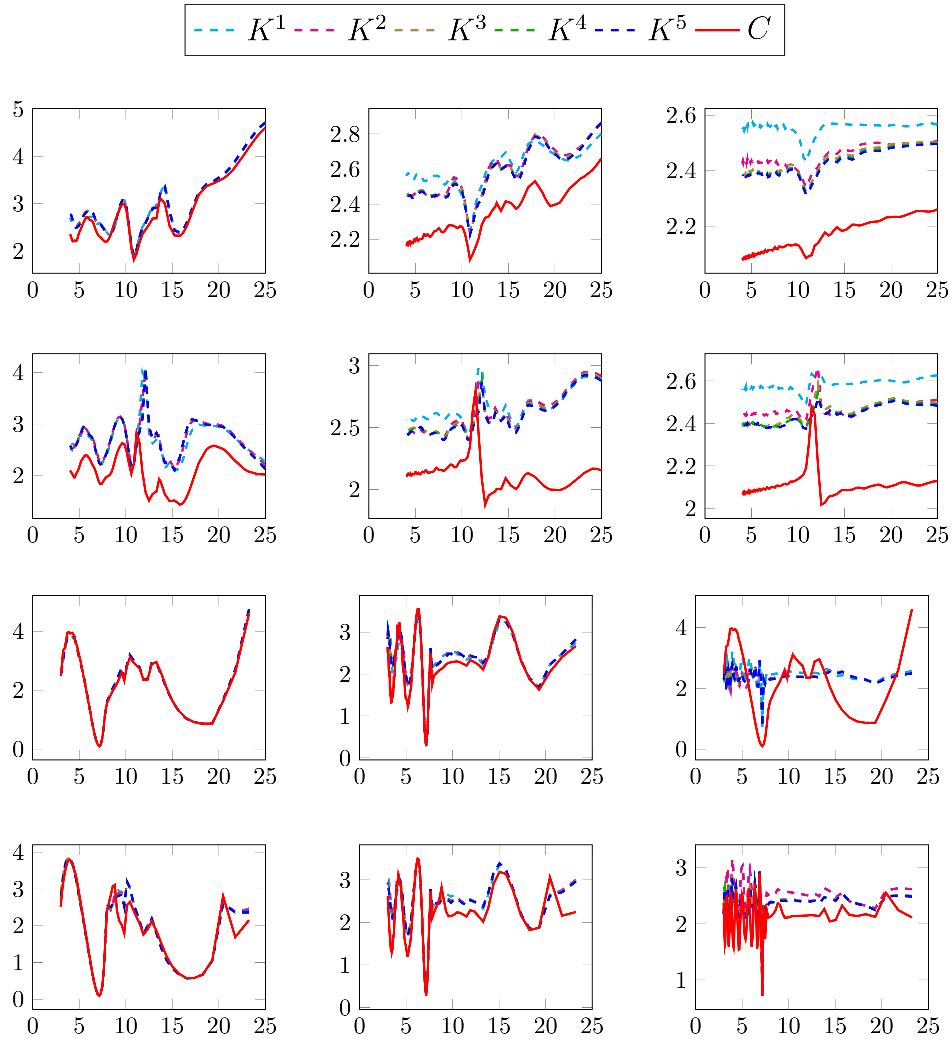

Figure 8: Averaged extinction efficiency $\widehat{Q}_e$ plots across the spectrum λ [µm]. The columns (from left) correspond to fractals F_6, F_{18}, and F_{54}, respectively. Top 2 rows correspond to silicon carbide; with first row for TE and second row for TM mode. The bottom 2 rows correspond respectively to silica; with third row for TE and fourth row for TM mode.

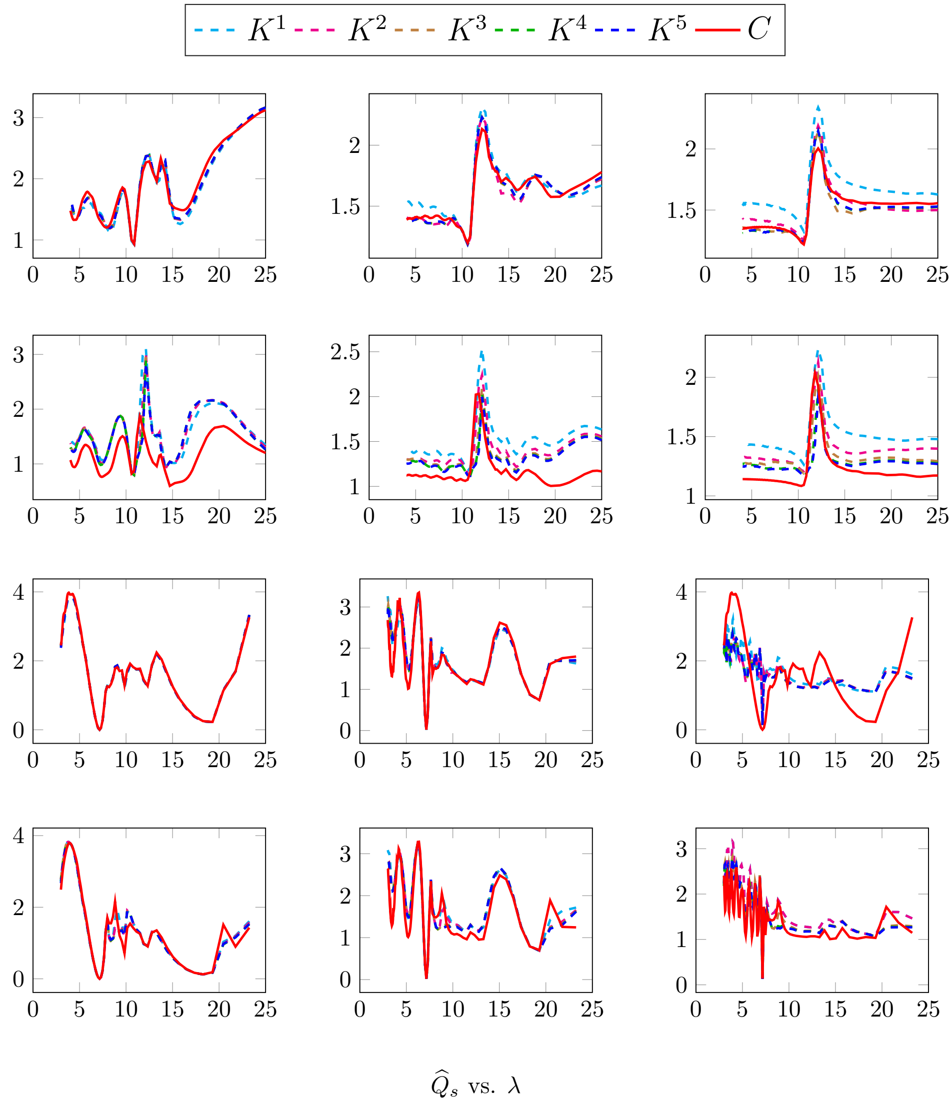

Figure 9: Averaged scattering efficiency $\widehat{Q}_s$ plots across the spectrum λ [µm]. The columns (from left) correspond to fractals F_6, F_{18}, and F_{54}, respectively. Top 2 rows correspond to silicon carbide; with first row for TE and second row for TM mode. The bottom 2 rows correspond respectively to silica; with third row for TE and fourth row for TM mode.

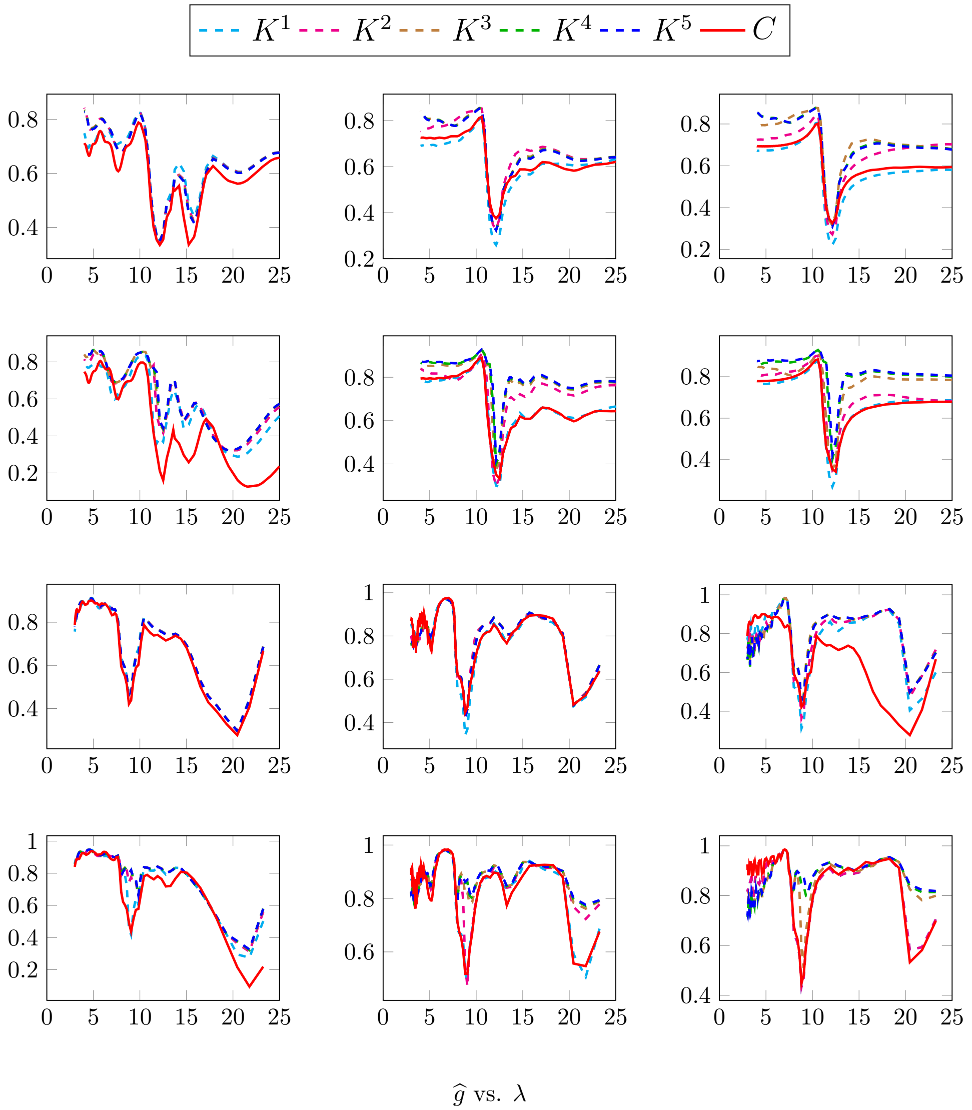

Figure 10: Averaged asymmetry parameter $\widehat{g}$ plots across the spectrum λ [μm]. The columns (from left) correspond to fractals F_6, F_{18}, and F_{54}, respectively. Top 2 rows correspond to silicon carbide; with first row for TE and second row for TM mode. The bottom 2 rows correspond respectively to silica; with third row for TE and fourth row for TM mode.

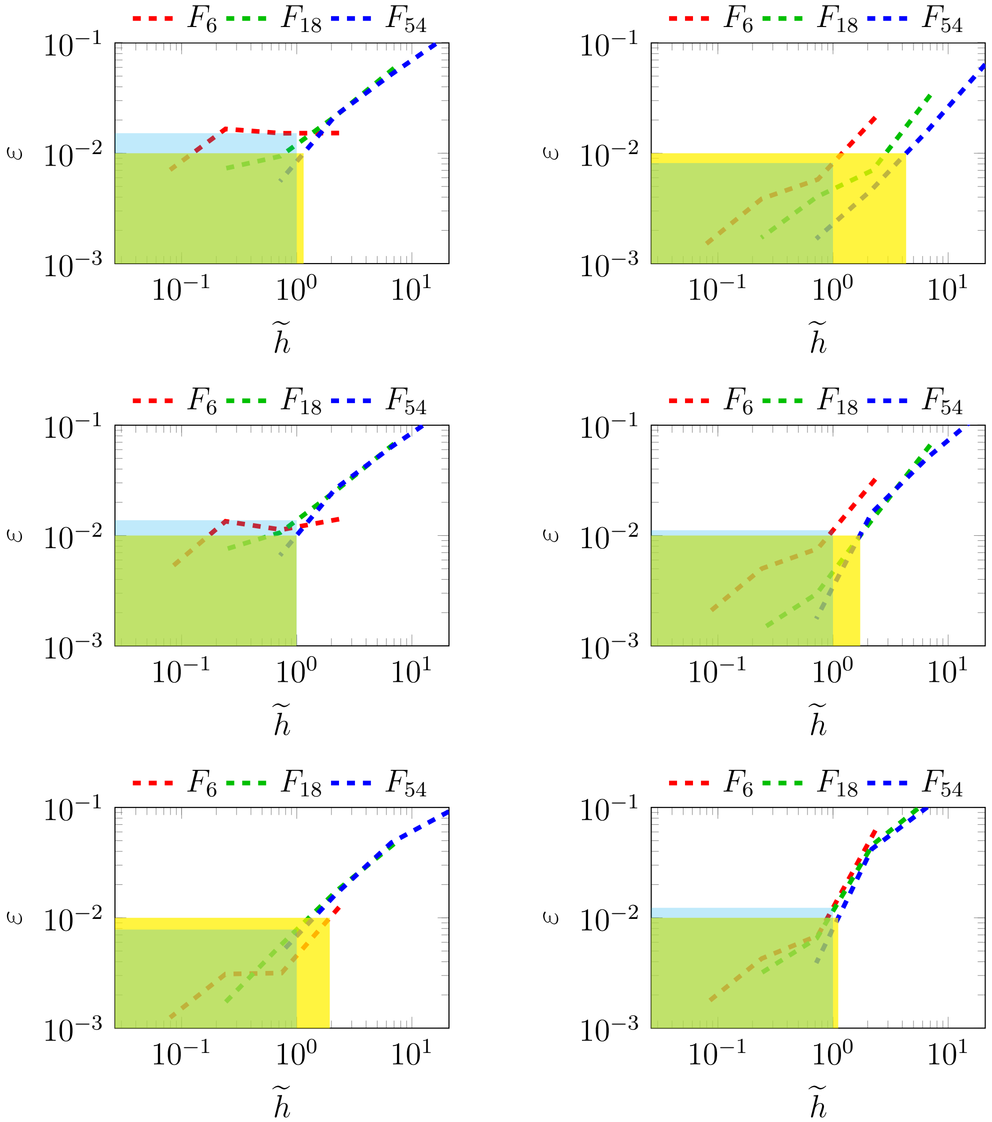

Figure 11: Wavelength-averaged normalized error ε plotted against $\widetilde{h}$, $\forall F_{d'}, d' = \{6, 18, 54\}$ for silica (left) and silicon carbide (right) fractals in the TE mode. Top row correspond to the error associated with the averaged extinction efficiency $\widehat{Q_e}$, second row to the averaged scattering efficiency $\widehat{Q_s}$ and third row to the averaged asymmetry parameter $\widehat{g}$. The shaded region in yellow shows the critical limit $\widetilde{h}_\varepsilon$ for 1 % error tolerance, and the one in blue shows the error associated with 1 µm resolution (please note that the union of yellow and blue colors yields the green color). Data pertaining to the TM mode is available in tables 2 and 3.

4. Conclusion

The prospect of undertaking a study on fractals – reliable for quantifying the roughness of complex objects, along with the finite element framework – capable of accurately modeling the generated complexities, provided some valuable insights regarding the ample textural details crucial for accurate radiative transport modeling. The critical limits tabulated in this study can serve as a lookup information for the studied materials across the spectrum, from where critical limit of textures needed for a required accuracy, or conversely the associated error while preferring an available resolution, can be quantitatively known beforehand. Quantitative limits of adequate textural details needed for an accurate radiative transport modeling estimated for the optically thick and thin medium in this work demonstrated the methodology to arrive at these limits, taking into account the orientation of the scatterers and polarization influences. For a desired level of accuracy ε preferred among diverse domains of interest, the critical limit $\widetilde{h}_{\varepsilon}$ of ample textural details relevant for the interested problem can differ. Briefly, It can be stated with confidence that $1\,\mu\mathrm{m}$ resolution is ample or adequate enough to provide accurate radiative transport predictions with error around $1\,\%$. The intensive numerical experiments modeled several possible physical scenarios, that the established quantitative limits pertain close to the physical reality. The finite element method modeled the studied complex fractals with relative ease and provided a wide variety of data plots to draw conclusions. The total field and far-field plots obtained served as ideal starting points which motivated the intense numerical experiments to further broaden the physical understanding. Thus, the finite element method proved to be the ideal tool to undertake similar future studies. It appears that investigations of this sort are the need of the hour, taking into account the modern compact industrial materials demanding maximum durability. This work served as a starting point for more general studies in 3D, where the computational challenges are more significant, and similar estimates can prove to be more crucial saving computational resources without compromising the accuracy. As only single scatterer was addressed in this study, future works addressing multiple scatterers can also further improve radiative transport modeling.

Acknowledgements

The authors acknowledge and express the owed gratitude to Le centre de calcul intensif des Pays de la Loire (CCIPL) and institut de calcul intensif (ICI, Centrales Nantes) for granting access to their parallel supercomputers, through the Glicid project number OG1810170. The authors thank the French Ministry of Higher Education and Research for funding this research. Dr. Mohd. Afeef Badri is also acknowledged for the fruitful discussions.

References

[1] M. Pelanconi, M. Barbato, S. Zavattoni, G. L. Vignoles, A. Ortona, Thermal design, optimization and additive manufacturing of ceramic regular structures to maximize the radiative heat transfer, Materials & Design 163 (2019) 107539.

[2] S. Guévelou, B. Rousseau, G. Domingues, J. Vicente, C. Caliot, Representative elementary volumes required to characterize the normal spectral emittance of silicon carbide foams used as volumetric solar absorbers, International Journal of Heat and Mass Transfer 93 (2016) 118–129.

[3] B. Rousseau, D. De Sousa Meneses, P. Echegut, J.-F. Thovert, Textural parameters influencing the radiative properties of a semitransparent porous media, International Journal of Thermal Sciences 50 (2) (2011) 178–186.

[4] K. Tang, R. A. Dimenna, R. O. Buckius, Regions of validity of the geometric optics approximation for angular scattering from very rough surfaces, International Journal of Heat and Mass Transfer 40 (1) (1996) 49–59.

[5] M. I. Mishchenko, Electromagnetic scattering by nonspherical particles: a tutorial review, Journal of Quantitative Spectroscopy and Radiative Transfer 110 (11) (2009) 808–832.

[6] J. Yamada, Radiative properties of fibers with non-circular cross sectional shapes, Journal of Quantitative Spectroscopy and Radiative Transfer 73 (2) (2002) 261–272.

[7] O. G. Ernst, M. J. Gander, Why it is difficult to solve Helmholtz problems with classical iterative methods, Springer Berlin Heidelberg, Berlin, Heidelberg, 2012, pp. 325–363.

[8] T. Mathew, Y. Favennec, B. Rousseau, Critical micro–textural details influencing radiative transport in heterogeneous materials, 2019, pp. 117–124. doi:10.1615/RAD-19.150.

[9] A. Milandri, F. Asllanaj, G. Jeandel, Determination of radiative properties of fibrous media by an inverse method – comparison with the mie theory, Journal of Quantitative Spectroscopy and Radiative Transfer 74 (5) (2002) 637–653.

[10] B. Rousseau, D. de Sousa Meneses, P. Echegut, M. Di Michiel, J.-F. Thovert, Prediction of the thermal radiative properties of an X-ray µ-tomographied porous silica glass, Appl. Opt. 46 (20) (2007) 4266–4276.

[11] S. Lallich, F. Enguehard, D. Baillis, Experimental Determination and Modeling of the Radiative Properties of Silica Nanoporous Matrices, Journal of Heat Transfer 131 (8).

[12] J. Petrasch, P. Wyss, A. Steinfeld, Tomography-based monte carlo determination of radiative properties of reticulate porous ceramics, Journal of Quantitative Spectroscopy and Radiative Transfer 105 (2) (2007) 180–197.

[13] I. Voznyuk, H. Tortel, A. Litman, 3-D electromagnetic scattering computation in free-space with the FETI-FDP2 method, IEEE Transactions on Antennas and Propagation 63 (6) (2015) 2604–2613.

[14] F. M. Kahnert, Numerical methods in electromagnetic scattering theory, Journal of Quantitative Spectroscopy and Radiative Transfer 79–80 (2003) 775–824.

[15] T. Wriedt, Light scattering theories and computer codes, Journal of Quantitative Spectroscopy and Radiative Transfer 110 (11) (2009) 833–843.

[16] M. Kahnert, Numerical solutions of the macroscopic maxwell equations for scattering by non-spherical particles: a tutorial review, Journal of Quantitative Spectroscopy and Radiative Transfer 178 (2016) 22–37.

[17] C. F. Bohren, D. R. Huffman, Absorption and Scattering of Light by Small Particles, Wiley-VCH Verlag GmbH, 2007. doi:10.1002/9783527618156.ch1.
URL `http://dx.doi.org/10.1002/9783527618156.ch1`

[18] H. Von Koch, G. Edgar, On a continuous curve without tangents constructible from elementary geometry, Classics on Fractals (Westview Press, 2004) pp 25 (1993) 45.

[19] F. Hecht, New development in FreeFem++, J. Numer. Math. 20 (3–4) (2012) 251–265.

[20] P. Jolivet, F. Hecht, F. Nataf, C. Prud'homme, Scalable domain decomposition preconditioners for heterogeneous elliptic problems, in: Proceedings of the International Conference on High Performance Computing, Networking, Storage and Analysis, SC '13, ACM, New York, NY, USA, 2013, pp. 80:1–80:11. doi:10.1145/2503210.2503212.
URL `http://doi.acm.org/10.1145/2503210.2503212`

[21] C. Geuzaine, J.-F. Remacle, Gmsh: a 3-D finite element mesh generator with built-in pre- and post-processing facilities, International Journal for Numerical Methods in Engineering 79 (11) (2009) 1309–1331.

[22] S. Balay, W. D. Gropp, L. Curfman McInnes, B. F. Smith, Efficient management of parallelism in object oriented numerical software libraries, in: E. Arge, A. M. Bruaset, H. P. Langtangen (Eds.), Modern Software Tools in Scientific Computing, Birkhäuser Press, 1997, pp. 163–202.

[23] J. A. Stratton, L. J. Chu, Diffraction theory of electromagnetic waves, Phys. Rev. 56 (1939) 99–107.